

# Test-Bed Simulations of Collisionless, Self-Gravitating Systems Using the Schrödinger Method

George Davies and Lawrence M. Widrow  
Department of Physics, Queen's University, Kingston, K7L 3N6, Canada

November 4, 2021

## Abstract

The Schrödinger Method is a novel approach for modeling numerically self-gravitating, collisionless systems that may have certain advantages over N-body and phase space methods. In particular, smoothing is part of the dynamics and not just the force calculation. This paper describes test-bed simulations which illustrate the viability of the Schrödinger Method. We develop the techniques necessary to handle “hot” systems as well as spherically symmetric systems. We demonstrate that the method can maintain a stable, equilibrium star cluster by constructing and then evolving a Plummer sphere. We also consider nonequilibrium initial conditions and follow the system as it attempts to reach virial equilibrium through phase mixing and violent relaxation. Finally we make a few remarks concerning the dynamics of axions and other bosonic dark matter candidates. The Schrödinger Method, in principle, provides an exact treatment of these fields. However such “scalar field” simulations are feasible and warranted only if the de-Broglie wavelength of the particle is comparable to the size of the system of interest, a situation that is almost certainly not the case for axions in the Galaxy. Therefore the Schrödinger Method treats axions in the same way as other collisionless particles. We challenge recent claims in the literature that axions in the Galaxy form soliton stars.

## 1 Introduction

Recently Widrow and Kaiser (1993) have developed a new numerical method for modeling self-gravitating, collisionless systems. Known as the Schrödinger Method (SM) this approach allows one to follow the evolution of such systems on a three-dimensional Eulerian grid and provides an alternative to both N-body and phase space methods.

Collisionless systems are ones in which the constituent particles move under the influence of the mean gravitational potential generated by all of the other particles. The state of a collisionless system is specified by a distribution function  $f = f(\mathbf{x}, \mathbf{v}, t)$  which gives the density of particles in phase space as a function of time.  $f$  is treated as a continuous fluid whose evolution is governed by the coupled Vlasov and Poisson equations (see e.g., Binney & Tremaine, 1986):

$$\frac{\partial f}{\partial t} = \sum_{i=1}^3 \left( \frac{\partial V}{\partial x_i} \frac{\partial f}{\partial v_i} - v_i \frac{\partial f}{\partial x_i} \right) \quad (1)$$

$$\nabla^2 V = 4\pi G \int d^3v f . \quad (2)$$

The Vlasov-Poisson pair must be solved numerically for most time-dependent systems of interest. One approach is to evolve  $f$  directly in phase space though efforts along these lines have had limited success primarily due to the large number of phase space dimensions typically involved. In contrast N-body or Particle methods (see, e.g., Hockney & Eastwood 1988) have been used successfully in virtually all astrophysical problems involving gravitational dynamics. The number of particles employed in an N-body simulation is typically many orders of magnitude less than the actual number of particles in the physical system one is modeling. This discrepancy can lead to unphysical effects due to “particle noise” such as two-body relaxation. Smoothing techniques alleviate this problem but at the cost of spatial resolution and care must be taken to choose a technique appropriate to the problem one is solving (Earn & Sellwood, 1995). On the other hand phase space methods, by explicitly constructing the smooth distribution function, avoid these difficulties.

The SM attempts to circumvent the problems of both phase space and N-body methods by encoding phase space information in a continuous position space function which we call  $\psi$ . Given an initial distribution function at time  $t_i$  we can find the distribution function at a later time  $t_f$  by the following general procedure:

$$f(\mathbf{x}, \mathbf{v}, t_i) \xrightarrow{\mathcal{M}} \psi(\mathbf{x}, t_i) \xrightarrow{\text{DEM}} \psi(\mathbf{x}, t_f) \xrightarrow{\mathcal{M}^*} f(\mathbf{x}, \mathbf{v}, t_f) . \quad (3)$$

Here DEM is the dynamical equation of motion for  $\psi$ ,  $\mathcal{M}$  maps  $f$  to  $\psi$ , and  $\mathcal{M}^*$  maps  $\psi$  to  $f$ . Ideally  $\mathcal{M}$  would be an invertible map with  $\mathcal{M}^* = \mathcal{M}^{-1}$  in which case the procedure would yield an exact solution to the Vlasov-Poisson pair.

With the SM,  $\psi$  is formally identified as a complex Schrödinger field obeying the coupled Schrödinger and Poisson equations:

$$i\hbar \frac{\partial \psi}{\partial t} = -\frac{\hbar^2}{2m} \nabla^2 \psi + mV\psi \quad (4)$$

$$\nabla^2 V = 4\pi G\rho . \quad (5)$$

$\mathcal{M}^*$  is the coherent state or Husimi transform (Husimi 1940), essentially the square of a windowed Fourier transform, and  $\mathcal{M}$  is a procedure to sample the initial distribution function to be discussed below.

In N-body simulations fictitious “superparticles” are used to provide a statistical representation of the distribution function. Imagine dividing position space into cells smaller than the scales of interest but larger than the interparticle spacing. The number of particles in each cell gives the (course-grained) density field while their velocity distribution provides the remaining information contained in  $f$ . The resolution in position space relative to velocity space can be controlled by adjusting the cell size. However the size of a phase space resolution element,  $\Delta\Omega$  is set by the number of particles  $N$  in the simulation:  $\Delta\Omega \simeq n\Omega/N$ . Here  $\Omega$  is the volume in phase space filled by the system (6 dimensional in general; 3 dimensional for spherically symmetric systems with angular momentum (see below)) and  $n$  is the number of particles required to have a reasonably accurate estimate of  $f$  at a given phase space point.

The SM shares some of these features. The de Broglie wavelength  $\lambda_{\text{deB}}$  for  $\psi$  enters as a model parameter and is chosen to be as small as possible, in general a few grid spacings. Position space is divided into regions smaller than the scales of interest but larger than  $\lambda_{\text{deB}}$  so that the WKB approximation applies. We can then think of  $\psi$  in this region as the superposition of plane waves

each of which represent different velocity streams in the distribution function. The correspondence principle guarantees that the “acceleration” of each stream is given by Newton’s Law. Since  $\psi$  is a continuous function there is no problem with particle noise. Moreover it is a function only of position rather than the phase space coordinates, and is therefore easier to work with. Formally, the resolution in phase space is set by the uncertainty principle. In practice it is set by the number of grid points  $N_g$ :  $\Delta\Omega \simeq n_g\Omega/N_g$  where  $n_g$  is the number grid points across a typical de Broglie wavelength. We therefore expect the SM to be competitive with particle mesh simulations in terms of resolution in phase space as a function of the number of grid points.

In a previous letter Widrow and Kaiser (1993) outlined the SM and presented simple illustrative simulations. In this paper we expand on that original work demonstrating, in a more quantitative way, the validity of the method. In particular we develop a new technique for handling “hot” systems (e.g. virialized systems) as well as systems with spherical symmetry. In Section 2 we review the SM and describe some of the new techniques implemented in this paper. Section 3 presents results of test-bed simulations. In particular we simulate a stable equilibrium star cluster (Plummer sphere) and a nonequilibrium cluster. Both simulations assume spherical symmetry but include angular momentum. In Section 4 we make a few remarks concerning recent work on axion dynamics and in particular challenge claims made in the literature which suggest that the “field” nature of axions is important for understanding their behaviour in the Galaxy. Section 5 offers a summary and some concluding remarks.

## 2 Schrödinger Method

### 2.1 From $\psi$ to $\mathcal{F}$

We use the coherent-state (Husimi 1940) representation to construct a phase space distribution function  $\mathcal{F}(\mathbf{x}, \mathbf{v})$  from  $\psi$ . Mathematically this is just the absolute square of a windowed Fourier transform. However, the physical content of this mapping is clearer when expressed in *bra-ket* notation:

$$\mathcal{F}(\mathbf{x}, \mathbf{v}) = |\langle \eta(\mathbf{x}, \mathbf{v}) | \psi \rangle|^2 \equiv |\Psi(\mathbf{x}, \mathbf{v})|^2 . \quad (6)$$

Here  $|\eta(\mathbf{x}, \mathbf{v})\rangle$  is the wavepacket for a single ‘particle’ centered on the phase space point  $(\mathbf{x}, \mathbf{v})$ ,

$$\langle \eta(\mathbf{x}, \mathbf{v}) | \mathbf{x}' \rangle = \left( \frac{1}{2\pi\hbar} \right)^{3/2} \left( \frac{1}{\pi\eta^2} \right)^{3/4} e^{-(\mathbf{x}-\mathbf{x}')^2/2\eta^2 - im\mathbf{v}\cdot\mathbf{x}'/\hbar} . \quad (7)$$

Equation (6) can then be seen as a prescription for decomposing  $\psi$  into Gaussian wavepackets with velocity  $\mathbf{v}$  and position  $\mathbf{x}$ . One can show, directly from the Schrödinger equation, that  $\mathcal{F}$  satisfies

$$\frac{\partial \mathcal{F}}{\partial t} = \sum_{i=1}^3 \left( \frac{\partial V}{\partial x_i} \frac{\partial \mathcal{F}}{\partial v_i} - v_i \frac{\partial \mathcal{F}}{\partial x_i} \right) + \left[ O\left(\frac{\eta^2}{L^2}\right) + O\left(\frac{\lambda_{\text{deB}}^2}{\eta^2}\right) \right] \frac{\partial \mathcal{F}}{\partial t} \quad (8)$$

(see, e.g., Skodje, Rohrs, & van Buskirk 1989) where  $L$  is the length scale over which the system varies and  $\lambda_{\text{deB}} \sim |\psi/\nabla\psi| \simeq \hbar/mv$  is the typically de Broglie wavelength of  $\psi$ . This equation reduces approximately to the Vlasov equation provided  $\lambda_{\text{deB}} \ll \eta \ll L$ .

Moments of the distribution function are calculated in the usual way (e.g.,  $\langle v^n \rangle = \int d^3 v v^n \mathcal{F} / \int d^3 v \mathcal{F}$ ). In particular the density field  $\rho$ , which is the source term for the potential  $V$ , is given by

$$\rho = \int d^3 v \mathcal{F} = \left( \frac{1}{\pi \eta^2} \right)^{3/2} \int d^3 \mathbf{x}' e^{-(\mathbf{x}-\mathbf{x}')^2/\eta^2} |\psi(\mathbf{x}')|^2 \quad (9)$$

Evidently  $\rho$  is found by applying a Gaussian filter to  $|\psi|^2$ , in effect, removing the high frequency modes. Of course what we are interested in is the potential  $V \sim \nabla^{-2} \rho$  and, since the inverse Laplacian also removes high frequency modes, we can safely replace  $\rho$  with  $|\psi|^2$  in equation (5). In practice we calculate  $V$  from  $\rho$  using FFT. Particle mesh simulations also use FFT to calculate the force from  $\rho$  and so the CPU time for this part of the calculation will be the same for the two methods.

## 2.2 From $f$ to $\psi$

We begin by sampling the distribution function, compiling a list of phase space points much as we would in an N-body simulation. The initial  $\psi$  is then taken to be the (incoherent) superposition of wavepackets centered on each of these points:

$$|\psi\rangle = \frac{1}{\sqrt{N}} \sum_{j=1}^N |\eta(\mathbf{x}_j, \mathbf{v}_j)\rangle . \quad (10)$$

The  $|\eta(\mathbf{x}_j, \mathbf{v}_j)\rangle$  are given by equation (7). The phase factor  $\exp(i\varphi_j)$  is included to insure that the wavepackets will add incoherently. While the physical motivation for this prescription is clear (we are just summing up ‘particles’) a more mathematical motivation is the completeness of  $|\eta(\mathbf{x}, \mathbf{v})\rangle$ :

$$\int d^3 \mathbf{x} \int d^3 \mathbf{v} |\eta(\mathbf{x}, \mathbf{v})\rangle \langle \eta(\mathbf{x}, \mathbf{v})| = I . \quad (11)$$

To see that this form provides a valid representation of  $f$  we compute  $\mathcal{F}(\mathbf{x}, \mathbf{v}) = \mathcal{M}^* (\mathcal{M}f)$ :

$$\mathcal{F}(\mathbf{x}, \mathbf{v}) = \frac{1}{N} \sum_{j=1}^N \sum_{k=1}^N \langle \eta | \eta_k \rangle \langle \eta_j | \eta \rangle \quad (12)$$

$$= \frac{1}{N} \sum_{jk} e^{-(\mathbf{x}-\mathbf{x}_j)^2/4\eta^2} e^{-(\mathbf{x}-\mathbf{x}_k)^2/4\eta^2} e^{-m^2\eta^2(\mathbf{v}-\mathbf{v}_j)^2/\hbar^2} e^{-m^2\eta^2(\mathbf{v}-\mathbf{v}_k)^2/\hbar^2} \Gamma_{jk} \quad (13)$$

where

$$\Gamma_{jk} = e^{-2im\mathbf{x}\cdot(\mathbf{v}_j-\mathbf{v}_k)/\hbar} e^{-2im\mathbf{v}\cdot(\mathbf{x}_j-\mathbf{x}_k)/\hbar} e^{2i(m(\mathbf{x}_j\cdot\mathbf{v}_j-\mathbf{x}_k\cdot\mathbf{v}_k)/\hbar+(\varphi_j-\varphi_k)/2)} . \quad (14)$$

Splitting this into a summation over equal and unequal indices we find,

$$\mathcal{F} = \frac{1}{N} \sum_{j=1}^N e^{-(\mathbf{x}-\mathbf{x}_j)^2/2\eta^2} e^{-2m^2\eta^2(\mathbf{v}-\mathbf{v}_j)^2/\hbar^2} + \mathcal{F}_1, \quad (15)$$

where  $\mathcal{F}_1$  is a summation over the interference terms and will tend to be small. It is instructive to compare this result with the usual N-body distribution function:

$$f(\mathbf{x}, \mathbf{v}) = \frac{1}{N} \sum_{j=1}^N \delta(\mathbf{x} - \mathbf{x}_j) \delta(\mathbf{v} - \mathbf{v}_j). \quad (16)$$

In the limit where the interference terms vanish equation (15) becomes equation (16) with the delta functions smoothed into Gaussians.

The discussion above reveals a key distinction between N-body methods and the SM: In an N-body simulation, smoothing is implemented only in the force calculation. The ‘particles’ in the SM are themselves treated as extended objects which evolve as would a distribution of particles (see below). Indeed, the particles/wavepackets in the initial distribution mix with one another and do not keep their identity as do particles in an N-body simulation. We therefore have, in effect, a form of *dynamical* smoothing.

### 2.3 Spherical Symmetry

We now specialize to spherical symmetry where phase space has three dimensions; radial coordinate  $r$ , radial velocity  $v_r$ , and angular momentum  $j = r\sqrt{v_\theta^2 + v_\phi^2}$ . The Vlasov and Poisson equations take the form:

$$\frac{\partial f}{\partial t} + v_r \frac{\partial f}{\partial r} + \left( \frac{j^2}{r^3} - \frac{\partial V}{\partial r} \right) \frac{\partial f}{\partial v_r} = 0 \quad (17)$$

$$\frac{\partial}{\partial r} r^2 \frac{\partial V}{\partial r} = 4\pi^2 G \int_{-\infty}^{\infty} dv_r \int_0^{\infty} dj^2 f \quad (18)$$

The derivation of equation (17) assumes implicitly that  $j \neq 0$ . (The Jacobian of the transformation from  $(\mathbf{x}, \mathbf{v})$  to  $(r, v_r, j)$  is singular for  $j = 0$ ). This in general does not present a problem so long as  $j$  is treated as a continuous variable. However for numerical work  $j$  is discretized and  $j = 0$  must be treated with care. Of course  $j$  can be viewed as a label since no differential operation with respect to  $j$  is ever performed. We can therefore write  $f(r, v_r, j) = f_j(r, v_r)$  and treat the evolution of the different  $f_j$ ’s separately.

For radial orbits ( $j = 0$ ) we write

$$f_0(r, v_r) \equiv \frac{F(r, v_r)}{r^2} \delta(v_\theta) \delta(v_\phi) \quad (19)$$

where  $F$  satisfies the following equation:

$$\frac{\partial F}{\partial t} + v_r \frac{\partial F}{\partial r} - \frac{\partial V}{\partial r} \frac{\partial F}{\partial v_r} = 0 \quad (20)$$

The Poisson equation is now

$$\frac{\partial}{\partial r} r^2 \frac{\partial V}{\partial r} = 4\pi G \int_{-\infty}^{\infty} dv_r \left( F + \pi \sum_{j^2} f_j \right) \quad (21)$$

where the sum over  $j^2$  is the discretized version of the integral over  $j^2$  in equation (18).

It is straightforward to extend the SM method to spherically symmetric systems with angular momentum. We construct a  $\psi_j$  for each  $f_j$  in the initial distribution function: For  $j = 0$  we have

$$\Psi_0(r, v_r) = C \int_0^{\infty} dr' e^{-(r-r')^2/2\eta^2} e^{-imv_r r'/\hbar} \psi_0(r') \quad (22)$$

where  $\psi_0$  obeys the equation

$$i\hbar \frac{\partial \psi_0}{\partial t} = -\frac{\hbar^2}{2m} \frac{\partial^2}{\partial r^2} \psi_0 + mV\psi_0 \quad ; \quad \left. \frac{\partial \psi_0}{\partial r} \right|_{r=0} = 0 \quad (23)$$

For  $j \neq 0$

$$\Psi_j(r, v_r) = C \int_0^\infty dr' e^{-(r-r')^2/2\eta^2} e^{-imv_r r'/\hbar} \phi_j(r') \quad (24)$$

$$i\hbar \frac{\partial \phi_j}{\partial t} = -\frac{\hbar^2}{2m} \frac{\partial^2}{\partial r^2} \phi_j + m \left( V + \frac{j^2}{2r^2} \right) \phi_j \quad ; \quad \psi_j|_{r=0} = 0. \quad (25)$$

The distribution function is then

$$r^2 |\Psi_0|^2 \simeq F \quad ; \quad |\Psi_j|^2 \simeq f_j \quad (26)$$

and the Poisson equation becomes

$$\frac{1}{r^2} \frac{\partial}{\partial r} r^2 \frac{\partial}{\partial r} V = 4\pi G \rho \quad (27)$$

where

$$\rho = |\psi_0|^2 + \frac{\pi}{r^2} \sum_{j^2} |\phi_j|^2. \quad (28)$$

Equation (28) emphasizes an important point: the  $j = 0$  phase space map gives a density while the  $j \neq 0$  map produces  $dM(j^2)/dr$ .

## 2.4 Numerical Preliminaries

It is convenient to write our equations in terms of the dimensionless quantities  $\mathbf{y} = \mathbf{x}/L$ ,  $\tau = t/T$ ,  $\chi = \psi/\sqrt{\rho_0}$ , and  $U = \frac{T^2}{L^2} V$  where  $L$  and  $\rho_0$  are the characteristic size and density of the system of interest. We then have

$$i \frac{\partial \chi}{\partial \tau} = -\frac{\alpha}{2} \nabla_y^2 \chi + \frac{1}{\alpha} U \chi \quad (29)$$

$$\nabla_y^2 U = \frac{3\pi^2}{32} \beta^2 \chi \chi^* \quad (30)$$

where  $\alpha \equiv \hbar T / \mu L^2$  and  $\beta^2 = 32G\rho_0 T^2 / 3\pi$ . We therefore have three dimensionless parameters,  $\alpha$ ,  $\beta$ , and  $\eta/L$ , at our disposal.  $\beta$  determines the choice of timescale:  $T = \beta T_d$  where  $T_d = \sqrt{3\pi/32G\rho_0}$  is the dynamical time. As we now show  $\alpha$  determines the size of the phase space region accessible in the simulation while  $\eta/L$  sets the relative resolution in position and velocity space. For simplicity consider one coordinate or two phase space dimensions. Suppose that our system comfortably fits inside a region of size  $\mathcal{L}$  in units of  $L$ . We discretize position space by choosing  $y_j = j\mathcal{L}/N$  where  $N$  is the number of gridpoints. Further suppose that the system, when viewed in velocity space, comfortably fits inside a region of size  $\mathcal{V}$  in units of  $L/T_d$ . The lattice spacing in velocity space is connected to the lattice spacing in position space in the usual way (see, e.g., Press, Flannery, Teukolsky, & Vetterling 1986), *i.e.* the velocity is proportional to the wave number of the FFT. For discrete points in velocity space we have (in units of  $L/T$ )  $u_k = 2\pi k \alpha / \mathcal{L}$  which implies that we should set  $\alpha = \beta \mathcal{V} \mathcal{L} / 2\pi N$ . Writing  $\alpha = \gamma \mathcal{L} / N$  where  $\gamma = O(1)$  we find  $\beta = 2\pi \gamma / \mathcal{V}$ . In practice we find that  $\gamma \simeq 5$  works well. For the Plummer sphere simulations below we take  $\mathcal{V} \simeq 5$  and  $\beta \simeq 2\pi$ .

The SM has the desirable feature that many quantities of interest can be calculated without having to actually construct the full phase space distribution function. We have already seen an

example of this when calculating  $\rho$ . In general, if the function does not depend on velocity, the velocity integral will collapse into a delta function.

$$\langle Q \rangle = \int d^3\mathbf{x} d^3\mathbf{v} Q(\mathbf{x}) \mathcal{F}(\mathbf{x}, \mathbf{v}) \quad (31)$$

$$= (2\pi\eta^2)^{-3/2} \int d^3\mathbf{x} d^3\mathbf{x}' e^{-(\mathbf{x}-\mathbf{x}')^2/\eta^2} Q(\mathbf{x}) |\psi(\mathbf{x}')|^2 \quad (32)$$

$$\simeq \int d^3\mathbf{x} Q(\mathbf{x}) |\psi(\mathbf{x})|^2 \quad (33)$$

In the case of velocity moments we can replace the  $v^n$  term with a corresponding derivative, perform a change of coordinates and integrate by part to get,

$$\langle v_j^n \rangle = \left(-i\frac{\alpha}{\beta}\right)^n \int d^3\mathbf{x} \left[ \frac{\partial^n}{\partial s^n} \left( e^{-s^2/4\eta^2} \psi(\mathbf{x} + s\hat{\mathbf{n}}_j/2) \psi^*(\mathbf{x} - s\hat{\mathbf{n}}_j/2) \right) \right] \Big|_{s=0}, \quad (34)$$

where  $\hat{\mathbf{n}}_j$  is the unit vector in the  $j$  direction. For the important case of  $\langle v^2 \rangle$  this expression reduces to,

$$\langle v^2 \rangle \simeq - \left(\frac{\alpha}{\beta}\right)^2 \int d^3\mathbf{x} \left\{ \psi(\mathbf{x}) \nabla^2 \psi^*(\mathbf{x}) \right\}, \quad (35)$$

where we have neglected a term proportional to  $\psi\psi^*$ , and have integrated by parts. This is just the usual quantum mechanical result  $\langle v^2 \rangle = \langle \hat{P}^2 \rangle / m^2$ .

Applying this to the case of spherical symmetry we then find,

$$\langle Q \rangle \simeq \sum_{j^2} \int_0^\infty dr Q(r) |\psi_j(r)|^2 \quad (36)$$

$$\langle v_r^2 \rangle \simeq - \sum_{j^2} \left(\frac{\hbar}{m}\right)^2 \int_0^\infty dr \psi_j^*(r) \frac{d^2\psi_j(r)}{dr^2}. \quad (37)$$

One can, of course, resort to the ‘brute force’ calculation of more complicated quantities,

$$\langle Q \rangle = \sum_{j^2} \int dr \int dv_r Q(r, v_r, j^2) \mathcal{F}_j(r, v_r). \quad (38)$$

The draw back of this approach is that it requires an  $O(N^4 \ln(N))$  calculation for each  $j$  plane. These calculations can be very time consuming, and it is time well spent looking for a short cut of the kind just presented.

### 3 Test-Bed Simulations

#### 3.1 Test Particles

As a first concrete example of the SM we will consider the motion of ‘test particles’ in a fixed Plummer sphere potential,

$$V(r) = -GM \left( L^2 + r^2 \right)^{-1/2}. \quad (39)$$

The SM analogue of a test particle is a single coherent state wave packet centered at some chosen point in phase space. Here we will examine the motion of four particles, two in the  $j = 0$  plane

and two in the  $j = 0.5$  plane. All four particles are taken to have zero initial radial velocity. The resulting initial wave functions are then just the sum of two Gaussians centered at the particle positions. The system is evolved by numerically solving equations (4) and (39), using the algorithm presented in Visscher (1991). This is an explicit algorithm and is at least a factor of three faster than the usual implicit ones. Figures 1 and 2 show the four particles moving in the Plummer sphere potential. These plots help to show the physical connection between  $\psi$  and  $\mathcal{F}$ , and the difference between the  $j = 0$  and  $j \neq 0$  phase space maps. The particle positions are given by the peaks of the wave function while the velocity information is encoded in the high frequency modes of  $\psi$ . From these plots one can see that the particles do follow the expected trajectories, justifying our choice of a spherical phase space map.

These plots also allow an interesting comparison of the SM and N-Body methods at a fundamental level. When one follows the evolution of an N-Body ‘superparticle’ it effectively carries with it a piece of phase space that has a fixed size and shape. When modeling systems in which mixing occurs these phase space blocks lead to unphysical coarseness of the distribution function. The evolution of the Schrödinger particles, on the other hand, carry with them a piece of phase space that has a *variable* shape and fixed volume. The motion of the test particles in figure 1 illustrates this point. The individual Schrödinger particles spread out along the phase space orbit in the same fashion as an equivalent distribution of point particles would. The conclusion is that fiducial SM particles can themselves take part in the phase mixing process.

We can also examine the evolution of an initially ‘cold’ (i.e., single velocity stream) distribution of test particles. The corresponding wave function is given by square root of the desired density multiplied by an appropriate phase factor:

$$\psi(\mathbf{x}) = \sqrt{\rho(\mathbf{x})}e^{-i\theta(\mathbf{x})} \quad (40)$$

where  $\nabla\theta = m\mathbf{v}'$ . This leads to the phase space distribution

$$\mathcal{F}(\mathbf{x}, \mathbf{v}) \sim \rho(\mathbf{x})e^{-\eta^2(m\mathbf{v}' - \hbar\nabla\theta)/\hbar^2}. \quad (41)$$

Compare this expression with the actual distribution function for a cold system:

$$f(\mathbf{x}, \mathbf{v}) = \rho(\mathbf{x})\delta(\mathbf{v} - \mathbf{v}'(\mathbf{x})) \quad (42)$$

The delta function has been replaced with a Gaussian of width  $\sim \hbar/\eta$ .

Figure 3 shows the phase space evolution of initially cold ( $v_r = 0$ ) test-particles with angular momentum  $j = 0.5$  (in units of  $L/T_d$ ) moving in the fixed potential of a Plummer sphere. The initial  $\psi$  is given by

$$\psi(r) = \sqrt{\left[ \int_{-\infty}^{\infty} dv_r f(r, v_r, j^2) \right] \Big|_{j=0.5}}, \quad (43)$$

where  $f$  is the Plummer sphere distribution function (see below). With no velocity pressure to support itself the system quickly begins to phase-mix its way to equilibrium.

### 3.2 Equilibrium Initial Conditions: The Plummer Sphere

Our first full-scale test-bed calculation is of an equilibrium star cluster, specifically a Plummer sphere. The distribution function for this model is given by

$$f(E) = \begin{cases} A|E|^{7/2} & \text{if } E < 0 \\ 0 & \text{otherwise} \end{cases} \quad (44)$$



where

$$E = \frac{1}{2} \left( v_r^2 + \frac{j^2}{r^2} \right) - \frac{GM}{L} \left( 1 + \frac{r^2}{L^2} \right)^{-1/2} \quad (45)$$

is the energy per unit mass,  $A = \frac{256}{35\pi^4} L^2 / G^5 M^5$ , and  $M$  is the total mass of the system.

Phase space is divided into  $N_j$  ( $r, v_r$ ) planes of constant  $j$  with each plane having  $N^2$  grid points. For the simulations that follow we set  $N = 1024$  and  $N_j = 25$ , with no  $j = 0$  plane. (The distribution function is sharply peaked in  $j^2$  at the origin, and it is difficult to consistently integrate  $\mathcal{F}$  with a small value for  $N_j$ . The lack of a  $j = 0$  plane is numerically consistent with a large value of  $N_j$ , where the  $j = 0$  plane would have a very small weight.) The planes are spaced equally in  $j$  although in general we can select planes at arbitrary values of  $j$ . We sample the set of  $N_j \times N^2$ ,  $\{r, v_r\}_i$  phase space points using the usual N-Body technique (see e.g. Hénon 1966). Figure 4 illustrates this sampling method. Here the set of sampled phase space points are shown for the  $j = 0.5$  and  $j = 1.0$  planes. With these points in hand one can algorithmically compute the coherent state summation to produce the set of  $N_j$  initial wave functions. Figure 5 shows the results of this construction. Here a typical phase space plane is shown, along with the generating wave function and the mass and velocity distributions for that plane. One should note that with the above choice of  $\eta$ , the  $r$  and  $v_r$  resolutions are very similar. If  $\eta$  were increased, corresponding to a larger smoothing window, the mass distribution would become smoother while the velocity distribution would become more jagged. In terms of the Schrödinger particles of Figure 1, the unit phase space particle would transform from a circle to an ellipse, becoming shrunken in the  $v_r$  direction and elongated in the  $r$  direction. All of these effects would be transposed for  $r$  and  $v_r$  if  $\eta$  were, instead, to be decreased.

The system is evolved by solving the coupled Schrödinger-Poisson system using the Visscher algorithm along with a potential solving routine based on Eastwood & Brownrigg (1979). Care must be taken to obtain the correct boundary condition at infinity when solving the Poisson equation on a finite grid. The routine that was implemented makes use of ‘padding’ to eliminate the effects of the grid boundary (at the expense of doubling the number of grid points). Figure 6 shows the mass and velocity distributions of the system in its initial state and after being evolved through 10 dynamical times. Figure 7 shows the  $j$  plane of figure 5 after 10 dynamical times. From these plots alone the system does appear to be stable. A quantitative measure of this is the virialization of the system: for a perfect Plummer sphere  $2T + W = 0$ . Where  $T$  is the total kinetic energy:

$$T = \frac{1}{2} \langle v_r^2 \rangle + \sum_{j^2} j^2 \int_0^\infty \left( \frac{1}{r^2} \right) |\psi_j|^2 dr , \quad (46)$$

and  $W$  is the potential energy of the system. The ratio  $2T/|W|$  was calculated during the evolution of the system over the course of 50 dynamical times. Figure 8 shows the evolution of  $2T/|W|$  for the system, with a similar curve obtained using a standard treecode (Barnes & Hut 1986) for reference. As can be seen from the plot, the SM Plummer sphere appears to be on par with the particle simulation.

### 3.3 Non-equilibrium Initial Conditions

As we saw in the last section, the Plummer sphere can be modeled quite well with only 25  $j$  planes. But how well can this method model a perturbed system? One can imagine a situation where the numerical representation of a system is sufficient near equilibrium but is too coarse to accurately

model an evolving system. Therefore, in order to test the true dynamics of the spherical SM we performed a destabilized Plummer sphere simulation (Rasio, Shapiro, & Teukolsky (1989) use this system to test their phase space code). The system was destabilized by reducing the  $v_r$  components of all the sampled Schrödinger particles by a factor of  $1/\sqrt{8}$ , giving  $2T/|W| = 17/24 \simeq 0.708$ . This was also done for the BH simulation, again with  $N = 1024$  particles. Figure 9 shows the evolution of  $2T/|W|$  for both of these simulations. As can be seen, both undergo the expected bounce and then begin to virialize and settle into a new equilibrium. Figure 10 follows one of the  $j$  planes through some of this process to illustrate the phase mixing that occurs.

## 4 Axion Dynamics and the Formation of Soliton Stars

The SM is applicable to any collisionless system regardless of what form the constituent particles take. (The same holds for N-body and phase space methods.) This is particularly relevant for studies of galactic halos and large scale structure where the dominant component of the mass density, the so-called dark matter, is in some unknown form. Dark matter candidates range from astrophysical compact objects such as black holes and brown dwarfs to elementary particles such as neutralinos. Still the dynamics of the system is independent of nature’s choice.

There is at least one exception to the above argument. If dark matter is in the form of a very light scalar field, then “quantum-mechanical” effects will enter into the dynamical equations of motion. In this case, the Schrödinger-Poisson pair provides the exact equations of motion (for non-relativistic motion) for the system. The mass  $m$  is now a true physical parameter determined by particle physics theory. Of course so long as the Compton wavelength for the field is much less than the scales of interest in the problem, the field will behave like collisionless matter.

Recently there has been considerable interest in soliton stars (for a review, see, e.g., Jetzer 1992). These objects are essentially self-gravitating compact objects made up of bosonic fields. The interest in soliton stars has been generated largely by the conjecture that dark matter may be bosonic. Indeed one of the most popular dark matter candidates is the axion, a pseudo-Nambu-Goldstone boson that arises in the PQ (Peccei & Quinn 1977) solution to the strong CP problem (Weinberg 1978; Wilczek 1978). Axions that are viable (there are constraints on the axion mass from cosmology, stellar evolution, and supernova studies (see, e.g., Kolb & Turner 1990)) have a mass  $\sim 10^{-5}$  eV and therefore a de Broglie wavelength in a galactic halo of  $\sim 10$  m. All this suggests that axions behave like any other dark matter candidate, i.e., like collisionless matter. However Seidel and Suen (1994) suggest that axions can form soliton stars. The question of whether this is indeed the case, or whether axions, like any other form of collisionless matter, form virialized clumps of matter, as in the axion miniclusters of Hogan and Rees (1988), is of fundamental importance in understanding whether or not axions are a viable dark matter candidate. Axions can annihilate into photons ( $AA \rightarrow \gamma\gamma$ ) provided the density is high enough. In the axion miniclusters of Hogan and Rees (1988) the density is  $10^7 \text{g/cm}^3$  and annihilation is unimportant. Alternatively the density in axion stars can be as high as  $10^{24} \text{g/cm}^3$ . At these densities, the annihilation is very efficient making the configuration unstable.

The question of course is whether axion stars ever form in the early Universe. A diffuse axion cloud must lose both angular momentum and energy if it is to form an axion star. Seidel and Suen (1994) find that a collapsing cloud can lose energy by radiating scalar material, a process they call gravitational cooling. However they only briefly mention the issue of angular momentum and carry out simulations of purely radial collapse. In these simulations the field collapses quickly

and an excited soliton star forms at the center and settles quickly by radiating scalar matter.

In what follows we argue that any reasonable amount of angular momentum will prevent the object from reaching the stage where gravitational cooling can take place. Consider an initial cloud of mass  $M$ , radius  $R_i$ , binding energy  $E_i \sim GM^2/R$ , and angular momentum  $J$ . A useful quantity is the dimensionless parameter

$$\lambda \equiv \frac{J|E|^{1/2}}{GM^{5/2}} \quad (47)$$

which is roughly the square root of the ratio between the rotational energy and the binding energy. As an object collapses,  $\lambda \propto R^{-1/2}$  provided there is no loss of angular momentum. We expect that this will indeed be the case at least in the initial collapse of the axion cloud.  $\lambda_f \lesssim 1$  in order for the final object to be gravitationally bound. We therefore require  $\lambda_i (R_i/R_f)^{1/2} \lesssim 1$  where  $R_f \simeq \hbar^2/\mu^2 GM$  is the radius of the final compact object. The bound is then

$$\lambda_i \lesssim 10^{-12} \left( \frac{10^{-5} \text{eV}}{m} \right) \left( \frac{M_\odot}{M} \right)^{2/3} \left( \frac{\rho}{\rho_{\text{halo}}} \right)^{1/6} \quad (48)$$

where  $\rho_{\text{halo}} = 0.008 M_\odot / pc^3$  is characteristic of the density of dark matter in the Galaxy. This is an incredibly small value for  $\lambda$ . It is widely believed that galaxies acquire angular momentum during formation from tidal interactions with nearby mass distributions. Typical values from both analytic and numerical work suggest that  $\lambda \simeq 0.01 - 0.1$  for galaxy-sized objects (see, e.g., Peebles 1969; Efstathiou & Jones 1979). The conclusion is that axionic matter, if indeed it does make up the dark halo, will have too much angular momentum to ever reach the densities required for gravitational cooling and soliton star formation.

## 5 Summary and Conclusion

This paper describes test-bed simulations of collisionless, self-gravitating matter using the SM. Included are several improvements over the earlier work by Widrow and Kaiser (1993). In particular we describe how to set up “hot” (e.g., virialized) systems. We also develop the techniques required to handle spherically symmetric systems with angular momentum which may be useful for studying violent relaxation and equilibrium star clusters. Of course the method is not restricted to problems with high degrees of symmetry. Our focus on spherically symmetric systems is mainly for illustrative purposes and, in hindsight, may not have been the best choice because of the special features of spherical coordinates. Widrow and Kaiser (1993) ran 2D cosmological simulations with results that were in excellent agreement with those from N-body simulations.

As discussed above, the SM is as efficient as a particle-mesh code in following the evolution of a system in phase space. One obvious improvement would be to use an adaptive grid and adaptive timestep to do the simulation. This could in principle make the method competitive with the widely used treecode of Barnes and Hut (1986).

The SM can be adapted to a wide variety of problems that have, as their central equation, Vlasov. For example Widrow (1996) has shown that the SM (actually the Klein-Gordon equation) can be used to simulate collisionless systems in general relativity. The method can also be applied to problems in electrodynamics that require information about the phase space structure of particles thereby providing an alternative to particle-in-cell codes and Eulerian Vlasov codes (see, e.g., Manfredi et al. 1995).

N-body techniques have been used in virtually all areas in astrophysics that require numerical simulations of collisionless matter. However despite years of research, there are still questions that arise over the validity and applicability of these simulations. Most of the questions center around smoothing, the technique used to construct a smooth density field from a system of discrete particles (Earn & Sellwood 1995). The SM provides an alternative where the “super-particles” of the N-body experiment are replaced by a continuous field. While the field may look like the superposition of particle-like wavepackets (indeed, this is how we set up our initial conditions) these wavepackets spread out in phase space as the system evolves. We therefore have a type of dynamical smoothing. Whether this dynamical smoothing has any real advantages over N-body methods remains to be seen.

*Acknowledgments* We would like to thank Martin Duncan and Jonathan Dursi for helpful discussions. Much of this work appears in a thesis by one of us (GD) submitted in partial fulfillment of a Master’s degree at Queen’s University. This work was supported in part by a grant from the Natural Sciences and Engineering Research Council of Canada.

## References

- Barnes, J. & Hut, P. 1986, *Nature* **324**, 446
- Binney, J. & Tremaine, S. 1987, *Galactic Dynamics* (Princeton: Princeton University Press).
- Earn, D. J. D. & Sellwood, J. A. 1995, *ApJ* **451**, 531
- Eastwood, J.W. & Brownrigg 1979, *J. Comp. Phys.* **32**, 24
- Efstathiou, G. & Jones, B. J. T. 1979, *MNRAS* **186**, 133
- Hénon, M. 1973, *A&A* **24**, 229
- Hockney, R. W. & Eastwood, J. W. 1988 *Computer Simulation Using Particles* (Bristol England: Adam Hilger)
- Hogan, C. J. & Rees, M. J. 1988, *Phys. Lett.* **B205**, 228
- Husimi, K. 1940, *Proc. Phys. Math. Soc. Jpn.* **22**, 264
- Jetzer, P. 1992, *Phys. Rep.* **220**, 163
- Kolb, E. W. & Turner, M. S. 1990 *The Early Universe* (Redwood City, California: Addison-Wesley Publishing Company)
- Manfredi, G. et al. 1995, *J. Comp. Phys.*, 121, 298
- Peccei, R. D. & Quinn, H. R. 1977, *Phys. Rev. Lett.* **38**, 1440
- Peebles, P. J. E. 1969, *ApJ* **155**, 393
- Press, W. H., Flannery, B. P., Teukolsky, S. A., & Vetterling, W. T. 1986 *Numerical Recipes* (Cambridge: Cambridge University Press)
- Rasio, F. A., Shapiro, S. L., & Teukolsky, S. A. 1989, *ApJ* **344**, 146.
- Seidel, E. & Suen, W. 1994, *Phys. Rev. Lett.* **272**, 2516
- Skodje, R. T., Rohrs, H. W. & VanBuskirk, J. 1989, *Phys. Rev.* **A40**, 2894.
- Visscher, P. B. 1991, *Computers in Physics*, Nov/Dec
- Weinberg, S. 1978, *Phys. Rev. Lett.* **40**, 223
- Widrow, L. M. & Kaiser, K. 1993, *ApJ* **416**, L71
- Widrow, L. M., [astro-ph/9607124](https://arxiv.org/abs/astro-ph/9607124)
- Wilczek, F. 1978, *Phys. Rev. Lett.* **40**, 279

## Figure Captions

**Fig. 1:** Test Particles: Here the Schrödinger test particles are moving in a fixed Plummer sphere potential with  $j = 0$ . The solid curves are the expected phase space trajectories for the respective initial conditions. The top four plots are taken at  $T = 0$  and the bottom four at  $T = 10.2 T_d$ . Here and below velocities are measured in units of  $L/T_d$  where  $T_d \equiv \sqrt{3\pi/32G\rho_0}$  (see text).

**Fig. 2:** Test Particles: Here the Schrödinger test particles are moving in a fixed Plummer sphere potential with  $j = 0.5$ . The top four plots are taken at  $T = 0$  and the bottom four at  $T = 10.2 T_d$ . The solid curves are the expected phase space trajectories for the respective initial conditions.

**Fig. 3:** Cold Distribution: The initial phase space distribution corresponds to the  $j = 0.5$  plane of a Plummer sphere with the velocity distribution suppressed. The system is out of equilibrium and rapidly collapses and begins to virialize.

**Fig. 4:** Sampling the Plummer Sphere: This figure shows the  $j = 0.5$  and  $j = 1.0$  planes of the Plummer sphere, each with its ‘N-Body’ sampled particles. This sampling is the last step prior to the construction of the initial wave functions  $\psi_j$ .

**Fig. 5:** The Equilibrium Plummer Sphere: This figure shows the initial wave function of a Plummer sphere  $j$  plane, along with the associated phase space distribution,  $\mathcal{F}_j(r, v_r)$ . The mass and velocity distributions were calculated directly from  $\mathcal{F}_j$ . The solid curves are the model distributions.

**Fig. 6:** The Equilibrium Plummer Sphere: This figure shows the initial mass and velocity distributions of the constructed Plummer sphere, along with the same distributions after the system was evolved through ten dynamical times. The dashed curves are the model distributions.

**Fig. 7:** The Equilibrium Plummer Sphere: This is the  $j$  plane of figure 5 after the system was evolved through ten dynamical times.

**Fig. 8:** The equilibrium Plummer Sphere: This figure shows the evolution of  $2T/|W|$  for the constructed Plummer sphere. The two curves are the results of the SM (line with points) and the BH tree code (with 1024 particles).

**Fig. 9:** The Destabilized Plummer Sphere: This figure shows the evolution of  $2T/|W|$  for the destabilized Plummer sphere. The two curves are the results of the SM (line with points) and the BH tree code (with 1024 particles).

**Fig. 10:** The Destabilized Plummer Sphere: This figure shows the evolution of  $j$  plane of the destabilized Plummer sphere. One can see that the system is phase mixing in a similar fashion to the cold system of figure 3.

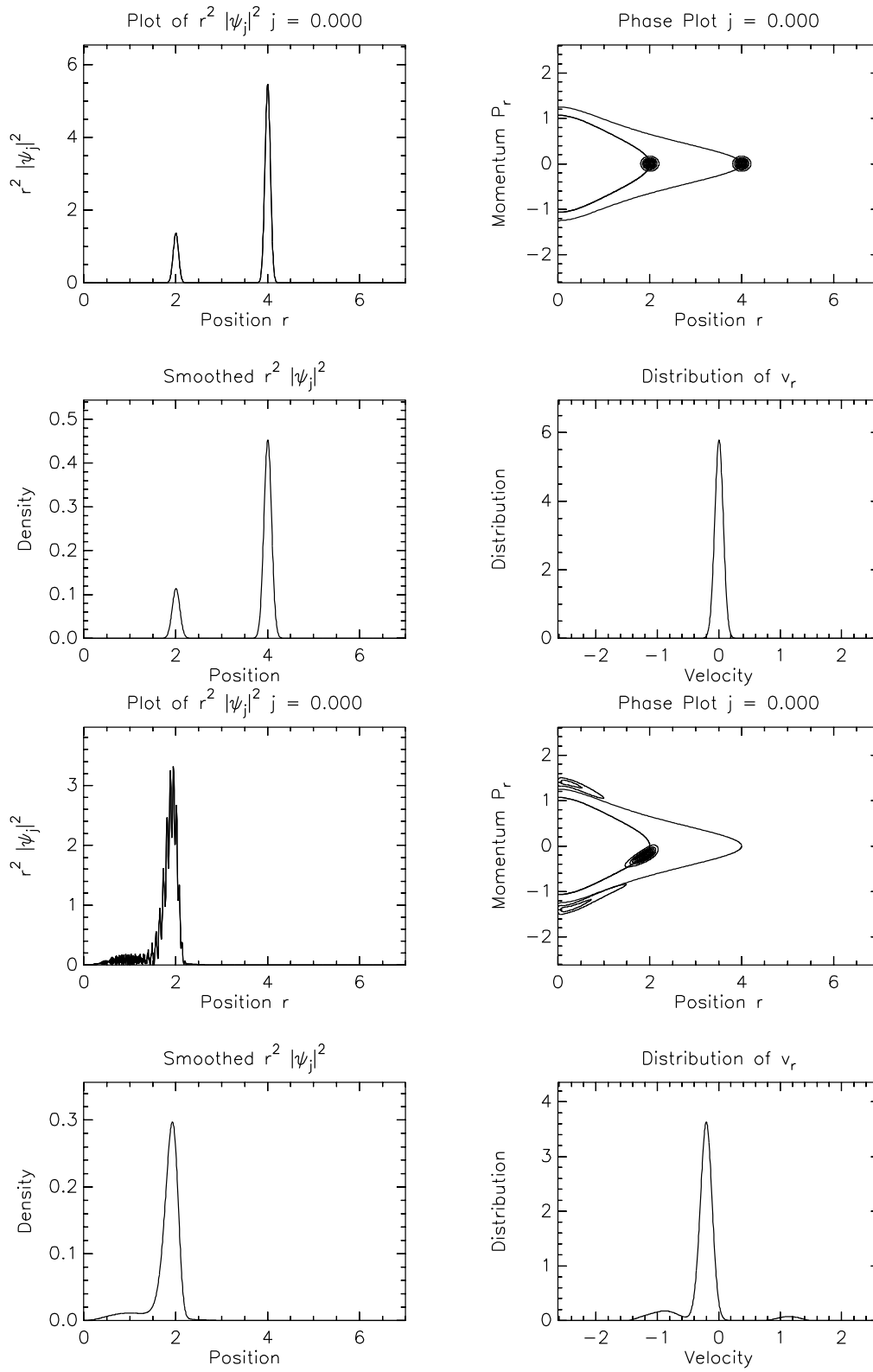


Figure 1:

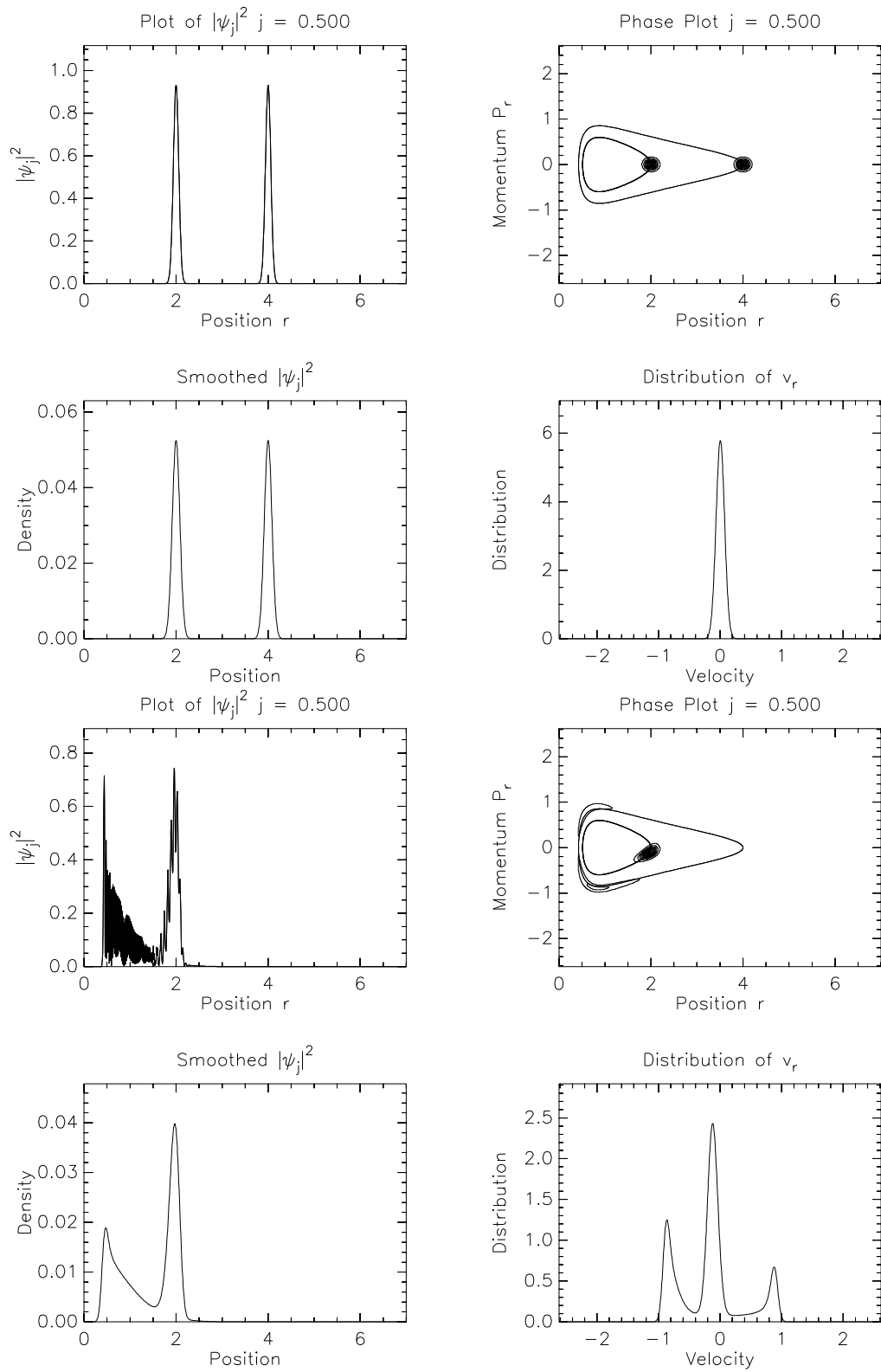


Figure 2:



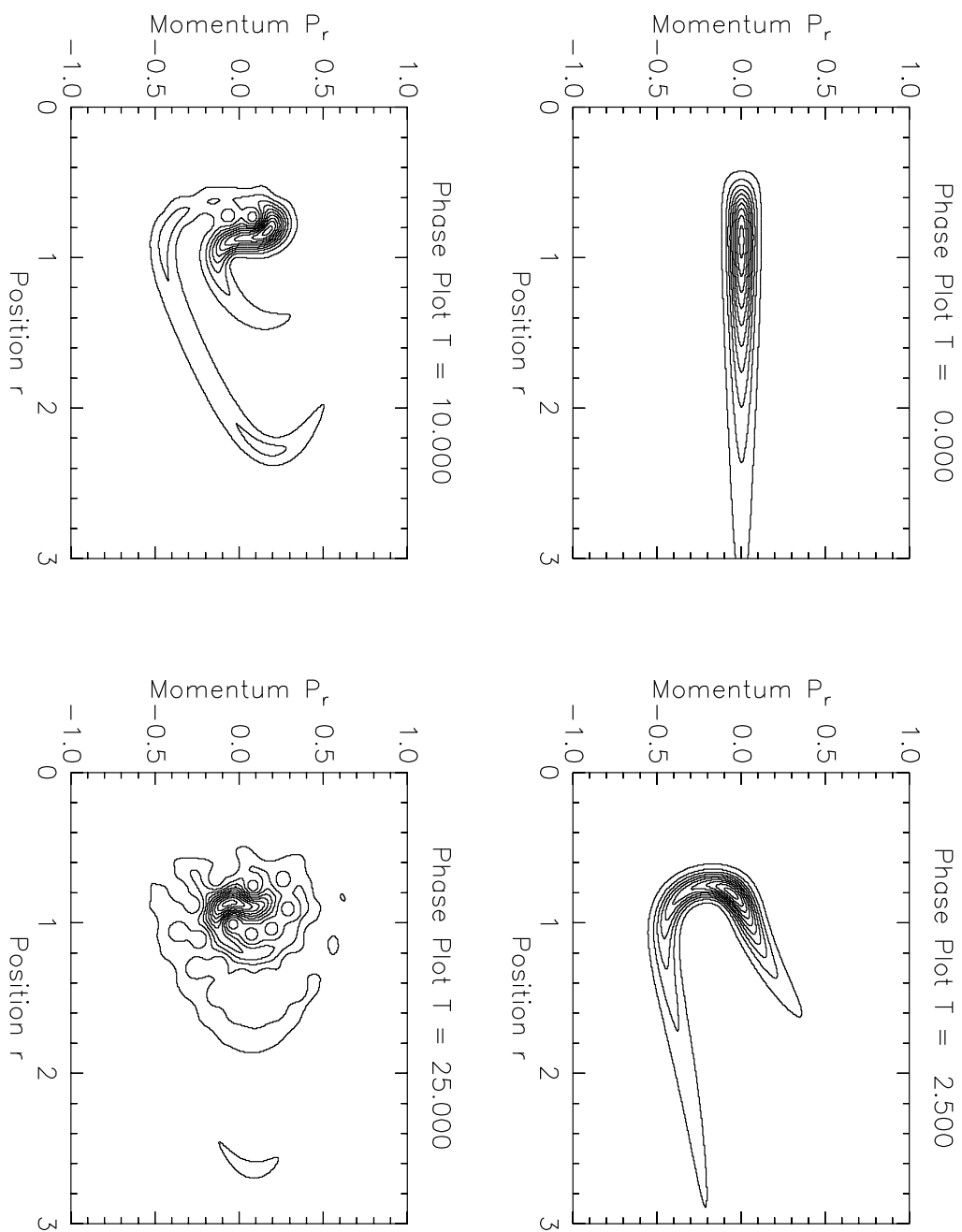


Figure 3:

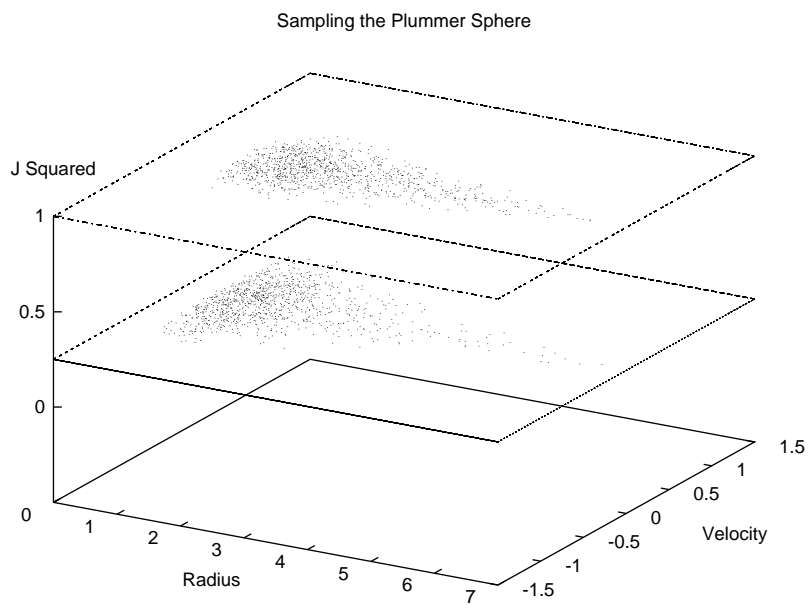


Figure 4:

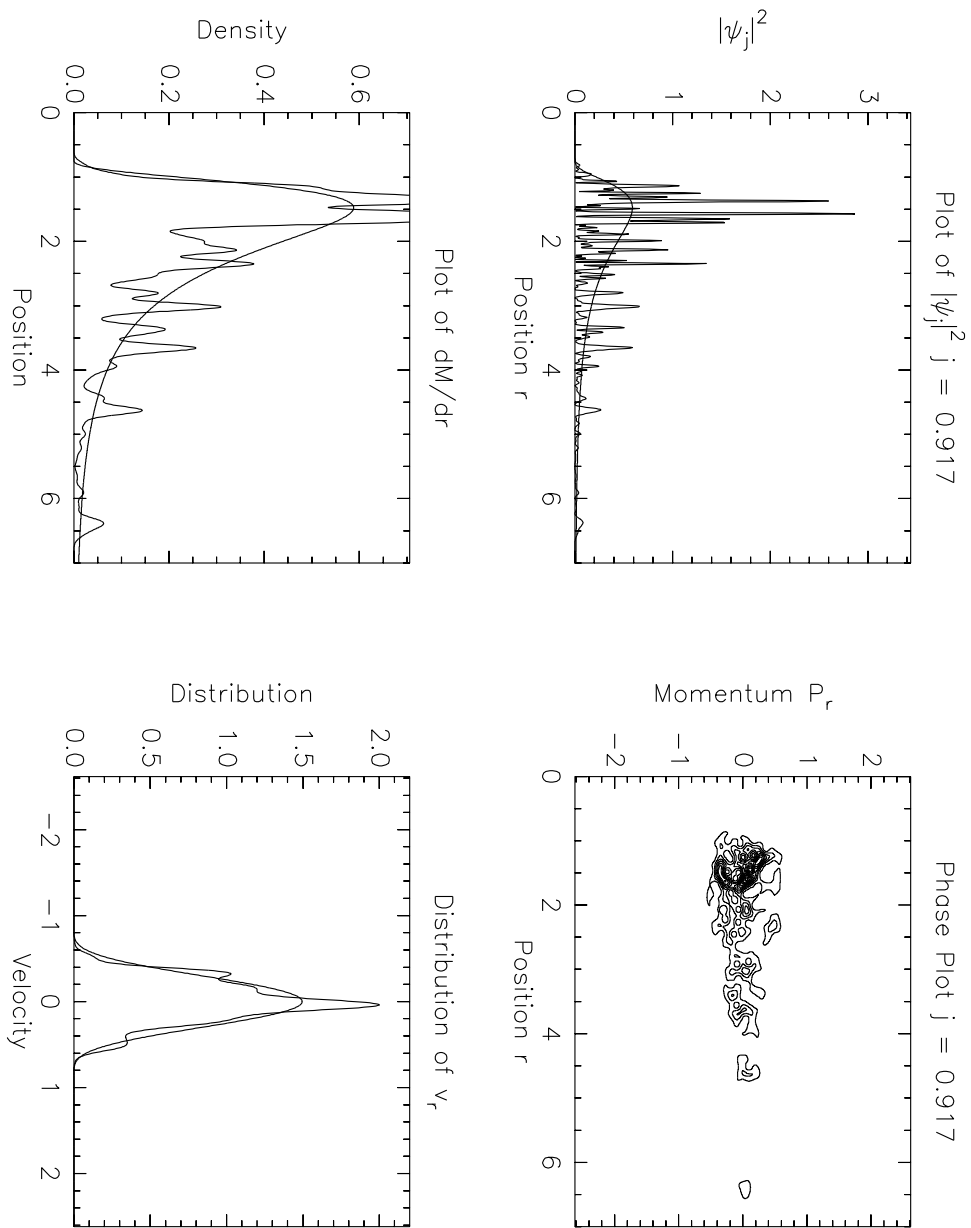
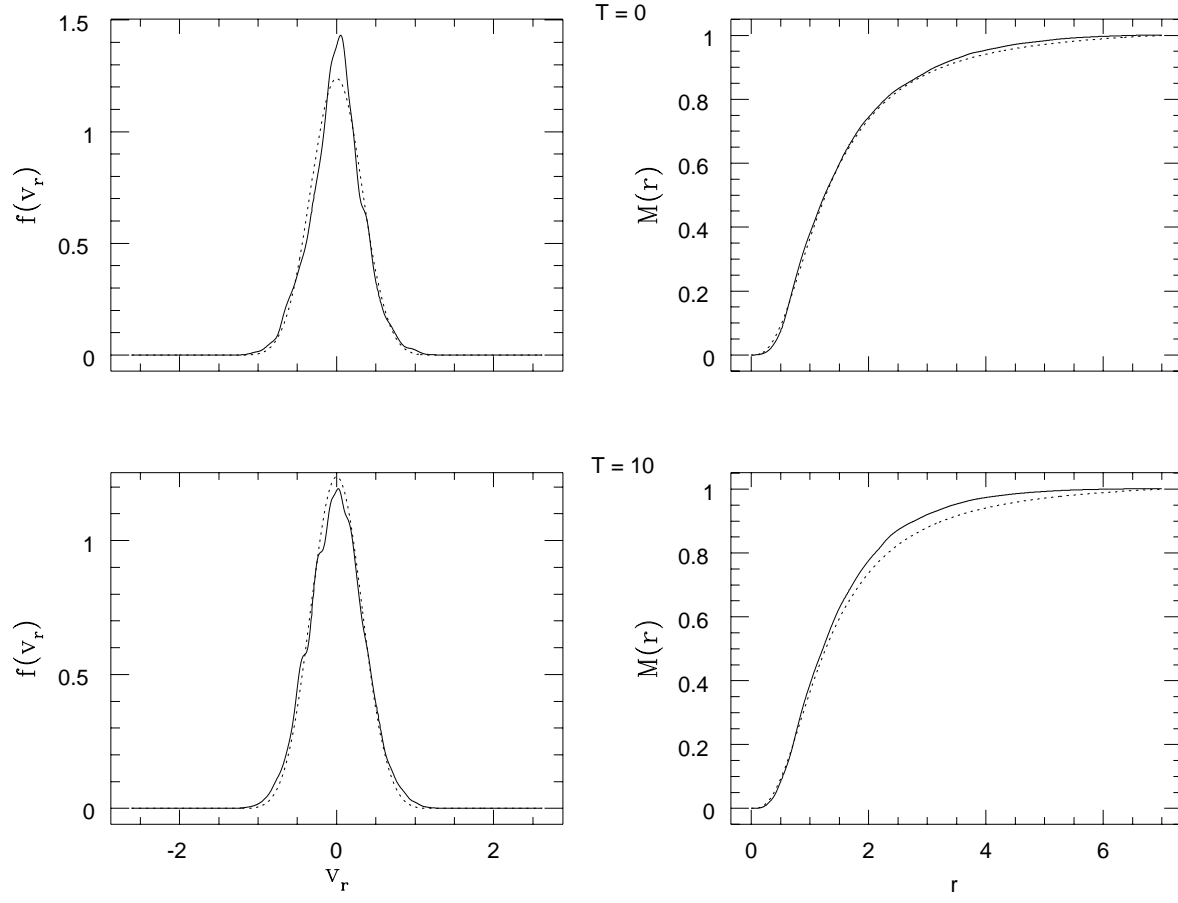


Figure 5:

Figure 6:



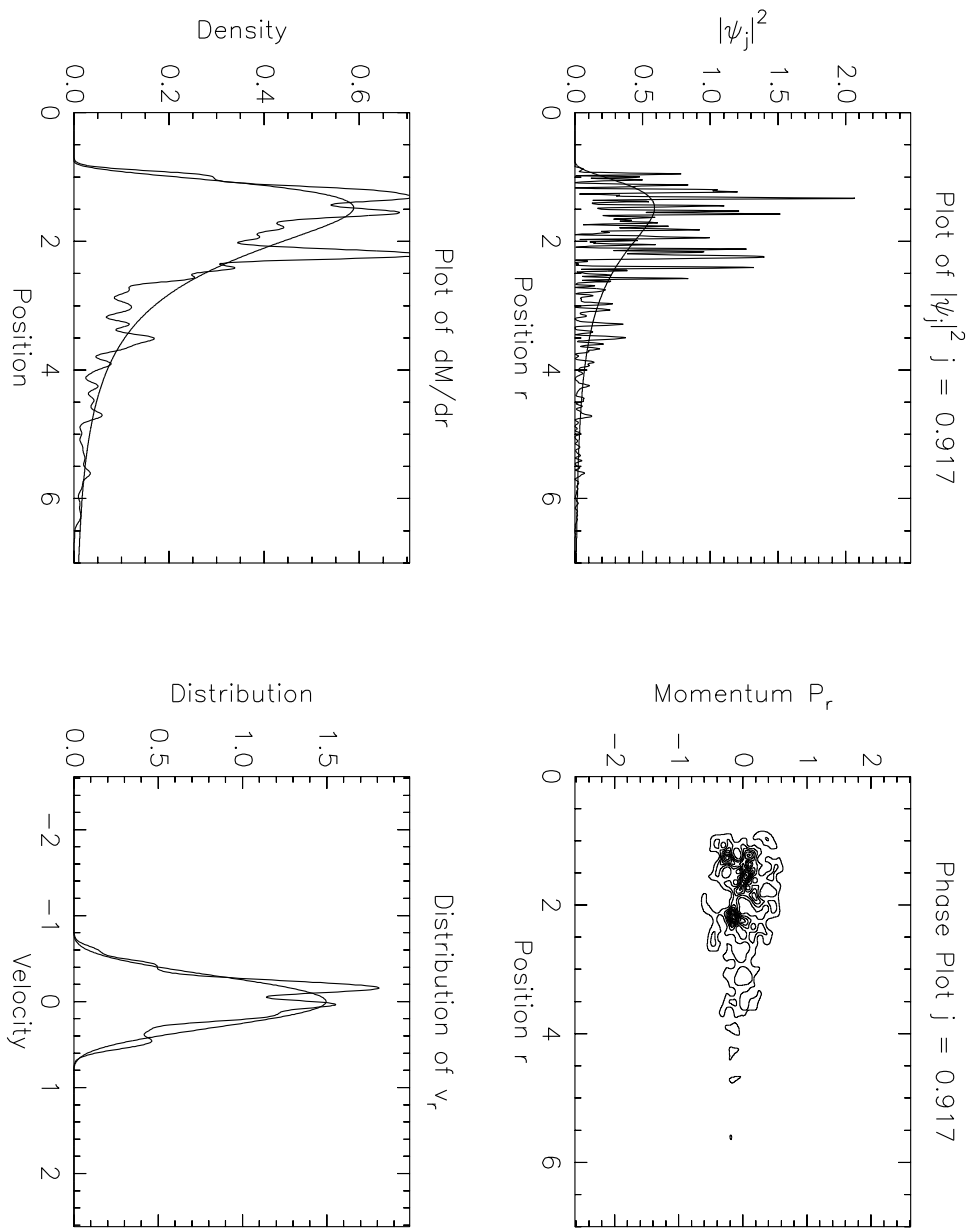


Figure 7:

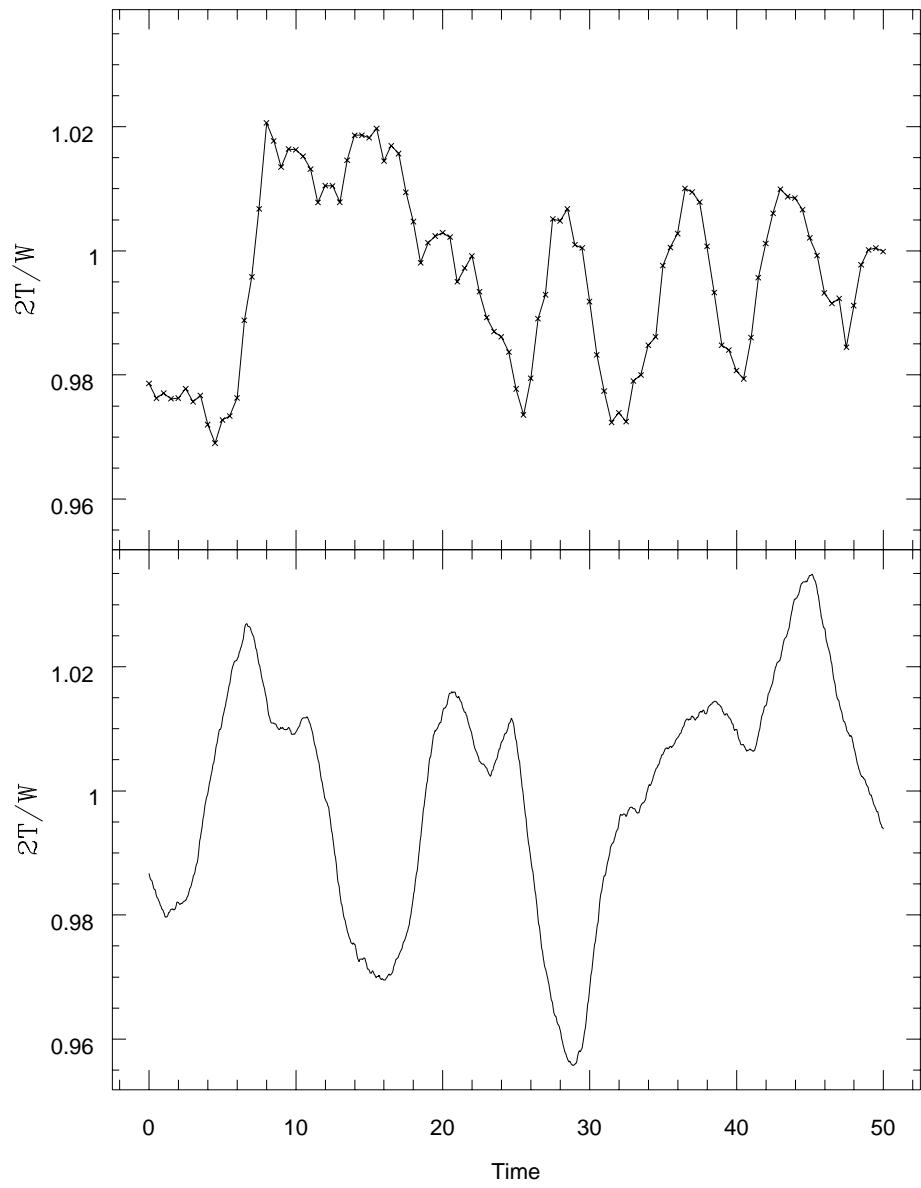


Figure 8:

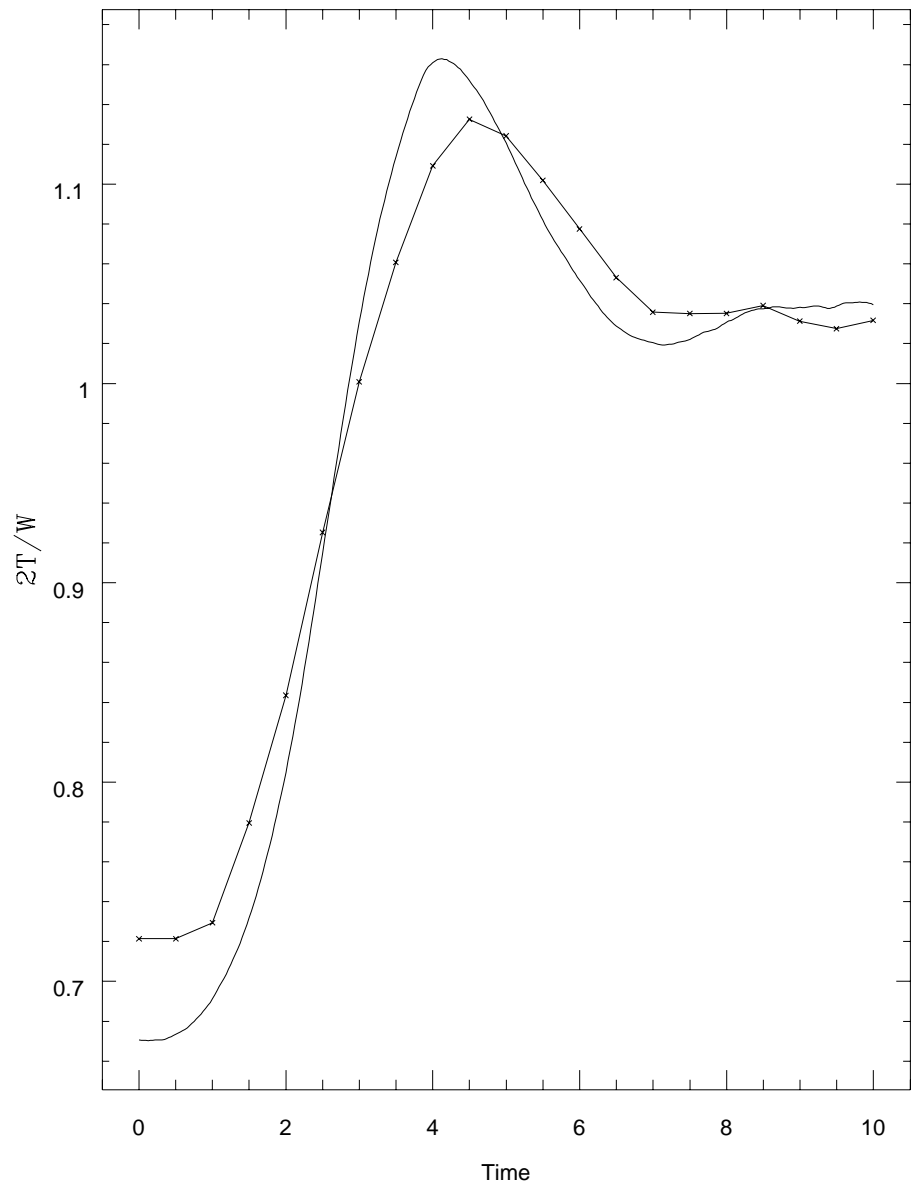


Figure 9:

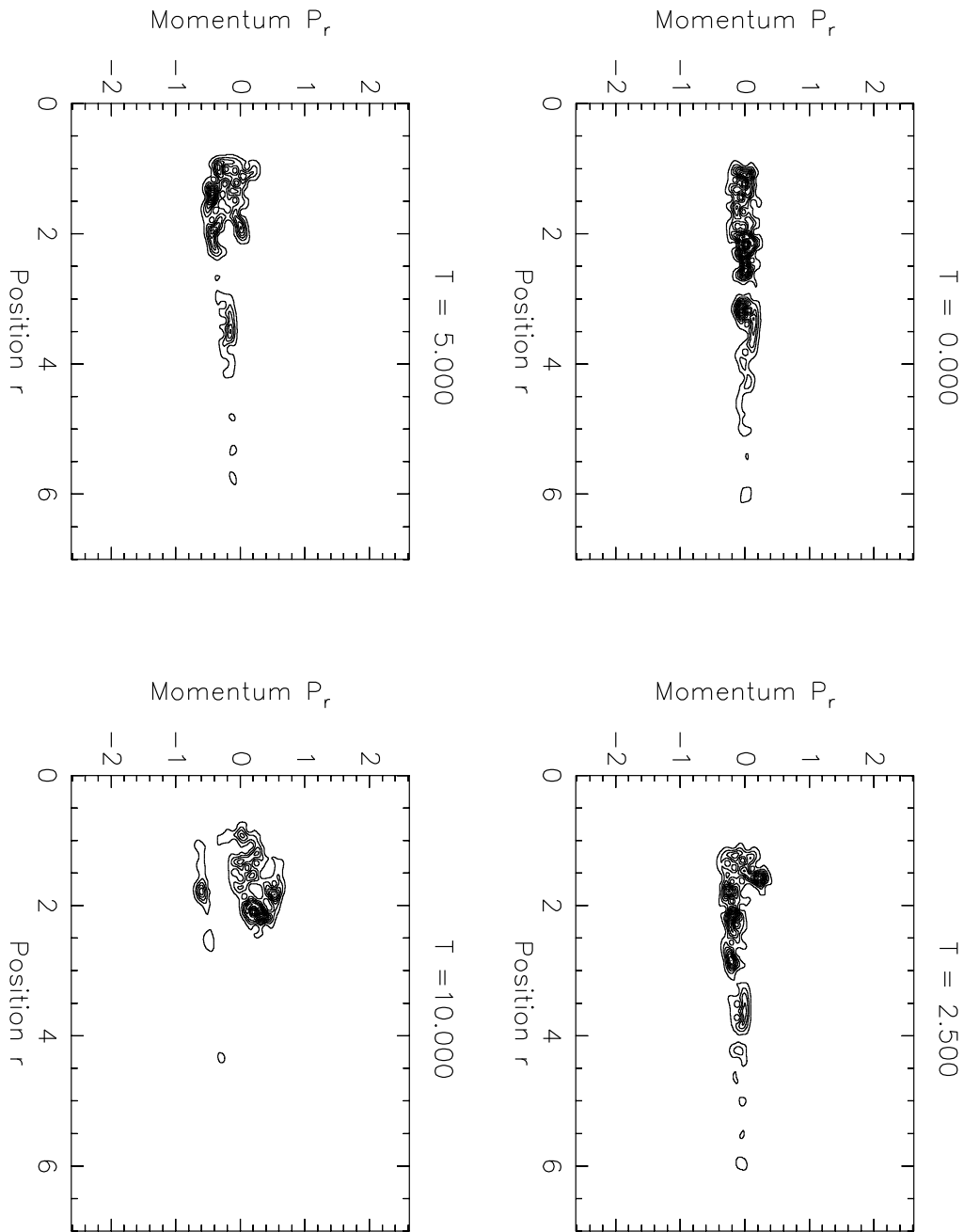


Figure 10: